Currents, waves and sediment transport around the headland of Pt. Dume, California

Douglas A. George[a],[*], John L. Largier[a], Curt D. Storlazzi[b], Matthew J. Robart[c], Brian Gaylord[a]

[a] *Bodega Marine Laboratory, University of California, Davis, Davis, CA, United States*
[b] *United States Geological Survey, Santa Cruz, CA, United States*
[c] *Vantuna Research Group, Occidental College, Los Angeles, CA, United States*

ARTICLE INFO

ABSTRACT

Sediment transport past rocky headlands has received less attention compared to transport along beaches. Here we explore, in a field-based study, possible pathways for sediment movement adjacent to Point Dume, a headland in Santa Monica Bay, California. This prominent shoreline feature is a nearly symmetrical, triangular-shaped promontory interior to the Santa Monica Littoral Cell. We collected current, wave, and turbidity data for 74 days during which several wave events occurred, including one associated with a remote hurricane and another generated by the first winter storm of 2014. We also acquired sediment samples to quantify seabed grain-size distributions. Near-bottom currents towards the headland dominated on both of its sides and wave-driven longshore currents in the surf zone were faster on the exposed side. Bed shear stresses were generated mostly by waves with minor contributions from currents, but both wave-driven and other currents contributed to sediment flux. On the wave-exposed west side of the headland, suspended sediment concentrations correlated with bed stress suggesting local resuspension whereas turbidity levels on the sheltered east side of the headland are more easily explained by advective delivery. Most of the suspended sediment appears to be exported offshore due to flow separation at the apex of the headland but may not move far given that sediment fluxes at moorings offshore of the apex were small. Further, wave-driven sediment flux in the surf zone is unlikely to pass the headland due to the discontinuity in wave forcing that causes longshore transport in different directions on each side of the headland. It is thus unlikely that sand is transported past the headland (specifically in a westerly direction), although some transport of finer fractions may occur offshore in deep water. These findings of minimal sediment flux past Point Dume are consistent with its role as a littoral cell boundary, although more complex multi-stage processes and unusual events may account for some transport at times.

1. Introduction and background

Rocky headlands are known to influence coastal flows and along-shore movement of suspended materials. For example, van Rijn (2010) notes that headlands can act as convergence points for wave energy, obstructions/convergence points for alongshore tide- and wind-induced currents, protrusions that generate nearshore re-circulation zones, semi-permeable boundaries for littoral drift, locations for seaward rip currents and offshore transport, as well as sites of spit formation and shoals originating from headland erosion. Especially important in the context of sediment movement is the capacity for headlands to impose littoral cell boundaries where spatial flow features can reduce or prevent along-coast transport of suspended materials (Habel and Armstrong, 1978; Stul et al., 2012; van Rijn, 2010). At the same time, the extent of blockage created by littoral cell boundaries (George et al.,

2015), and the specific particle sizes for which any given boundary applies, remain open questions (Limber et al., 2008).

1.1. Hydrodynamics at headlands

Flow patterns at headlands are important for characterizing sediment transport, in particular how eddies, wakes, and jets can convey suspended material. Black et al. (2005) listed factors that may influence headland eddy growth, size, shape, and decay: complexity of coastline and bathymetry, bottom friction, unsteadiness of flow, horizontal tidal excursion, tidal current direction, and horizontal eddy viscosity. Further insights are available from work on island wakes, although Magaldi et al. (2008) noted that the presence of a coastline up/downstream of the obstacle and a shallow sloping bottom boundary create key differences between wakes created by headlands versus islands. The

coastline exerts friction on the alongshore flow, therefore decreasing the Reynolds number (Verron et al., 1991). In addition, the shelf and potential for nearshore stratification alter fluid dynamics (e.g., potential vorticity, baroclinic instabilities) as well as formation of lee waves (Freeland, 1990; Klinger, 1993; MacCready and Pawlak, 2001). Signell and Geyer (1991) examined numerically how length/width aspect ratio, drag, and far-field tidal velocity affect flow around an idealized headland, whereas Davies et al. (1995) assessed the roles of friction, velocity, and geometry. Guillou and Chapalain (2011) examined how flow past a headland was affected by the interaction of wave and current boundary layers and the resulting reduction of current intensity from wave-induced roughness. Other field studies focused on sediment transport have addressed sandbanks rather than alongshore flow. Bastos et al. (2002) described the effect of tidal stirring (tidal residual eddies) at a headland in the United Kingdom and presented conceptual models of bed shear stress in an inner convergence zone with subsequent transport toward the headland, and an outer zone with subsequent transport from the headland. Transient tidal eddies were observed to exchange sand between a sandbank and offshore around Cape Levillain, Australia (Berthot and Pattiaratchi, 2006). Even in wave-dominated locations, tidal flow and transport are noticeable, such as at Cape Rodney, New Zealand, where the sediment type on the bed coarsens substantially at the apex of the headland compared to the sandbank deposits off-apex (Hume et al., 2000).

The interaction of tidal flows with headlands has received the majority of attention for producing headland flow but waves and wave-current interactions can also be important. Waves cause sediment transport through several mechanisms (Soulsby, 1997) with efficacy depending on grain size (or degree of flocculation for fine sediment). Because wave energy is focused at headlands, wave-driven longshore transport may be important. Short (1999) illustrated sand bypassing a headland as a multi-stage process with longshore transport from waves being the main driver. Further, Goodwin et al. (2013) estimated that 80% of longshore transport and headland bypassing along the New South Wales of Australia occurs in water depths less than 4 m. Similar shallow-water transport has been suggested in the Santa Barbara region of California based on years of beach profile observations (D. Hoover, USGS, pers. comm.).

1.2. Conceptual sediment transport pathways

These two primary drivers (waves and currents) have several possible behaviors when interacting with headlands. Persistent currents can show three patterns at the apex of the headland: (A) flow can separate and form a jet directed offshore, (B) flow can separate and reattach to the coastal boundary downstream, forming an eddy inshore, or (C) flow can remain attached to the coastal boundary (Fig. 1). Flow separation has been explored by Wolanski et al. (1984) and Pattiaratchi et al. (1987). Depending on flow and headland geometry, flow patterns may differ between flow in one direction versus the other. Wave forced flows exhibit more small-scale structure that interacts with the larger current behaviors described above. George et al., (2018) used numerical modeling that varied the incident wave angle and resulting patterns of flow and transport around differently shaped headlands designed to imitate naturally occurring ones. The relative angle between the propagation angle of incident waves and the shoreline alignment was found to produce three fundamental patterns: (i) waves approach perpendicularly to the shore, impinging directly on the headland and driving divergent longshore flows on either side of it, (ii) waves approach from one side of the headland driving strong longshore flow on one side and creating a wave shadow and discontinuity in longshore transport on the other side, or (iii) when a headland has an apex angle smaller than 90°, waves at a steep angle can drive continuous flow around the headland – no wave shadow and no reversal in wave forcing. Each of these scenarios will show distinctive flow directions or wave parameters in observational records as detailed in Table 1.
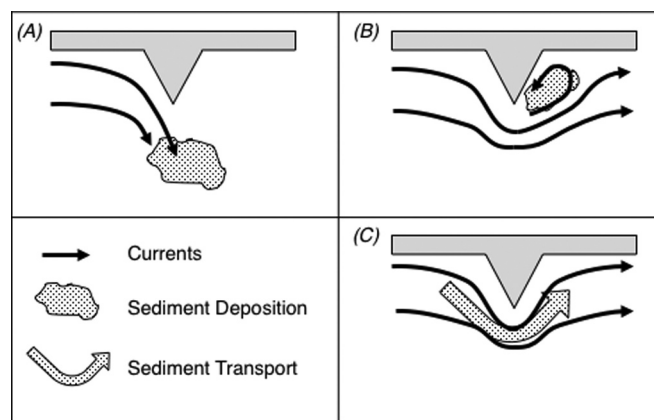

Fig. 1. Flow transport possibilities around a headland: (*A*) flow separates from nearshore with export of sediment offshore; (*B*) flow separates and forms a headland eddy with a downstream deposition zone; (*C*) flow remains attached with continuous transport past the headland.

Together, wave-driven longshore currents and low-frequency currents driven by tides, winds and pressure gradients can move sediment mobilized by breaking waves and super-critical bed shear stress at a headland.

1.3. Study motivation

The aim of this study was to examine how sediment flux can vary spatially and temporally around a rocky headland on a coast where waves, tides and wind-driven currents are important. Specific objectives were: (1) to examine potential sediment transport at a rocky headland under different oceanographic conditions, e.g., spring and neap tides and different wave events; (2) to contrast conditions and resultant transport on opposite sides of the headland; and (3) to assess the likelihood of the headland to be a barrier to sediment transport.

2. Study site

Several criteria were used to select an appropriate field location for a generalized study of sediment flux around a headland. The desired headland needed to be nearly symmetrical to minimize geomorphological complexity and imitate the design of theoretical numerical models, to have published transport rate estimates from prior work, and to be a sandy system as muddy systems at headlands are not as common globally. Point Dume in Malibu, California, satisfied these criteria. It is also at the center of a decades-old debate about its effectiveness as a barrier within the Santa Monica Littoral Cell.

Pt. Dume is the largest headland inside Santa Monica Bay (Fig. 2), a sub-bay of the Southern California Bight. The geology and geomorphology of the Pt. Dume headland region is also influenced by a headland-submarine canyon complex. George et al. (2015) defined the nearly symmetrical triangular-shaped Pt. Dume to be 12 km long (west-east alongshore axis) and 4 km in amplitude (north-south cross-shore axis). The entire headland lies south of the Malibu Coast Fault and is comprised of a mix of Holocene, Pleistocene and Tertiary era rock and alluvial deposits. The apex is predominantly sandstone. The head of Dume Submarine Canyon lies immediately offshore, approximately 1 km from the headland.

Generally, subtidal currents flow poleward in the Bight, driven by the Southern California Eddy and Southern California Countercurrent, both offshoots of the equatorward flowing California Current System (Hickey, 1992; Noble et al., 2009). Within Santa Monica Bay however, Hickey et al. (2003) describe a clockwise gyre that accounts for a mean inflow to the bay (eastward current) along the northern shoreline past Point Dume. The shelf in Santa Monica Bay is 30–40 km long with a

Table 1
Concepts for headland circulation and sediment flux.

Scenario	Flow or wave characterization	Sediment response	Observational criteria
A	Separation and jet	Offshore export	Accelerated flow along one side of headland and at apex in same direction with negligible counter flow on opposite side; convergence zones possible at apex
B	Separation and reattachment	Near-continuous sediment transport and small downstream deposition zone	Flow follows shape of headland from one side, across apex, and approaches downstream coastline; counter flow immediately adjacent to opposing side
C	Attached	Continuous transport around headland	Flow follows shape of headland from one side, across apex, and along opposite side

maximum cross-shelf width of < 20 km. Internal tides that transition to tidal bores are important (Noble et al., 2009). The Bight and Santa Monica Bay are sheltered from north and northwest waves by Pt. Conception 160 km west of Pt. Dume; the Channel Islands also block much of the westerly swell. Xu and Noble (2009) described the wave climate inside the Bight as moderate with winter storm waves from the west although long-period ($T_p > 15$ s) swell enters from the south and southwest primarily during summer and autumn. In their analysis of 23 years of hourly buoy data in the Santa Monica Basin, Xu and Noble (2009) calculated a significant wave height (H_s) mean of 1.3 m and 1.1 m for winter and summer, respectively; the 95th percentile in winter increases to 2.3 m and 1.6 m in the summer. Because of the predominant wave and current direction, net sand transport has traditionally been hypothesized to be to the east and south along the curving shore of Santa Monica Bay (Leidersdorf et al., 1994).

Santa Monica Bay and its littoral cell have received prior attention from sediment researchers. Habel and Armstrong (1978) produced the first explicit boundaries of the Santa Monica Littoral Cell, for which they defined a termination at Pt. Dume and the adjacent Dume Submarine Canyon. Leidersdorf et al. (1994) presented a sharp contrast between the narrow unnourished beaches along the northern shore and the heavily altered central and southern shorelines of the bay. A key assumption in the latter analysis was that sediment moved around Pt. Dume in an eastward direction. Patsch and Griggs (2007) estimated a total sand supply of 569,000 m³/yr moving in the system, of which 402,000 m³ (71%) is from beach nourishment actions. They also identified that natural sand supply from rivers and bluffs has been reduced by 13% from dams and coastal armoring projects. This last study also

expanded the littoral cell to 91 km in length by extending the boundary to the west, which incorporated Pt. Dume as a sub-cell within the overall system – implying that Point Dume does not function as a boundary for sediment transport. Some researchers have attempted to quantify how the point-canyon complex affects alongshore transport of sand, with estimates ranging from 10% to 90% of sediment bypassing the headland and being lost in the canyon (Inman, 1986; Knur and Kim, 1999; Orme, 1991). The lack of precision in this estimate reduces its interpretational value.

3. Methods

The observational elements of this study were developed to address the objectives on a localized scale. The design of the study examined spatial and temporal variability through three questions based on the study objectives: (1) Are there differences in sediment transport under different oceanographic conditions? (2) Are there discernable differences in the forcing conditions on either side of the headland and at the apex that could represent differences in sediment transport? (3) If those differences exist, are they substantial enough to disrupt sediment transport around the apex of the headland?

3.1. Field data collection

The field program sampling design was informed by methods for the study of marine sediment dynamics described by Soulsby (1997), by prior research at headlands in Australia (Berthot and Pattiaratchi, 2006), the United Kingdom (Bastos et al., 2002) and California
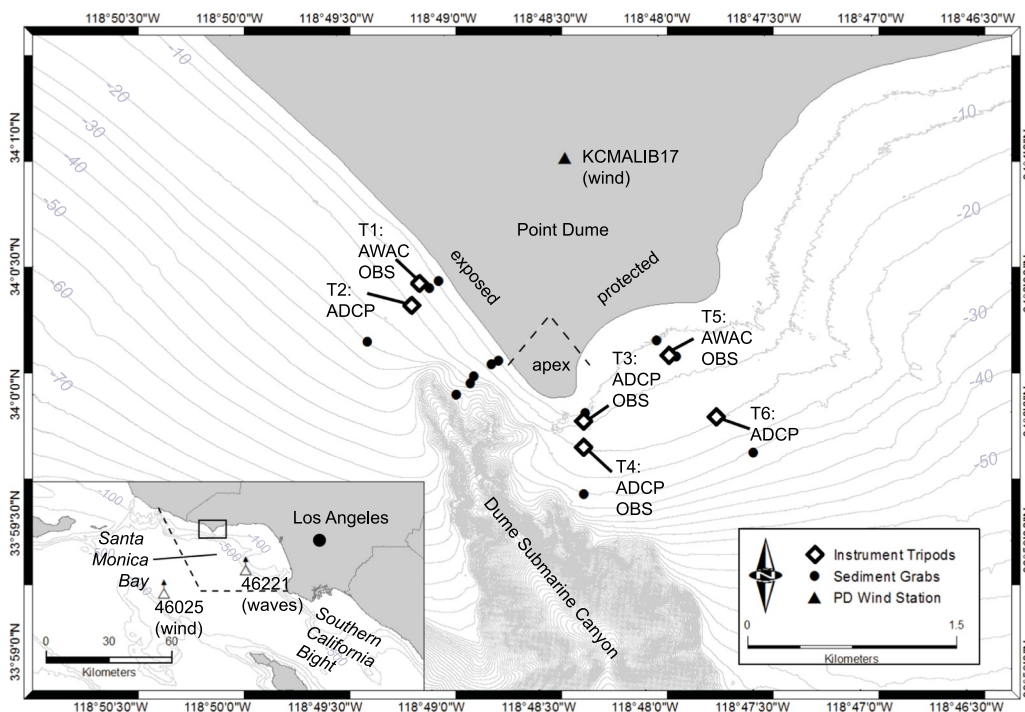

Fig. 2. Site map of Point Dume, Malibu, California, with instrument tripod and sediment grab locations. Instruments were deployed from 21 September to 6 December 2014. Data from the NDBC buoys (inset) and the Weather Underground weather station (KCMALIB17) were downloaded over the same time frames as the deployment for regional wind and wave conditions. Bathymetry is from NOAA in 5 m contour intervals, with the Dume Submarine Canyon indicated.

Table 2
Instrument datasets.

Location	Longitude	Latitude	Depth (m)	Measurements	Instruments
Deployed for Study					
T1	− 118.818150	34.00768	8	Currents, waves Turbidity	AWAC (1000 kHz) OBS
T2	− 118.818710	34.00624	15	Currents	ADCP (1200 kHz)
T3	− 118.805200	33.99892	11	Currents Turbidity	ADCP (1200 kHz) OBS
T4	− 118.805154	33.99725	16	Currents Turbidity	ADCP (1200 kHz) OBS
T5	− 118.798630	34.00328	10	Currents, waves Turbidity	AWAC (1000 kHz) OBS
T6	− 118.794850	33.99937	17	Currents	ADCP (300 kHz)
National Data Buoy Center, NOAA					
B1 (#46221)	− 118.633	33.855	363	Waves	Waverider Buoy
B2 (#46025)	− 119.053	33.749	5 m above sealevel	Wind	Advance Modular Payload System (AMPS) (1 Hz)
Weather Underground					
PD Wind (KCAMALIB17)	− 118.807	34.016	65 m above sealevel	Wind	Davis Vantage Vue

(Roughan et al., 2005), and by recent work on the "coastal boundary layer" that exists immediately beyond the surf zone (Nickols et al., 2012). Data were collected on oceanographic forcing and resulting local hydrodynamics (tides, waves, and currents), composition of the bed, and suspended sediment transport. Fieldwork was conducted from the end of summer to the beginning of winter (19 September 2014 to 6 December 2014) to capture a diversity of wave, current, and storm conditions.

3.1.1. Instrumentation

The study region was divided into three zones: the wave-exposed west side of the headland, the apex, and the wave-sheltered east side of the headland. Instrument packages were deployed at a pair of locations along three transects normal to the shoreline (Fig. 2, Table 2) to measure tides, waves, currents, and suspended sediment. Four Teledyne RDI Acoustic Doppler Current Profilers (ADCP) and two Nortek Acoustic Wave And Currents (AWAC) instruments were programmed to measure the three-dimensional components of current velocity (U, V, W, m/s) every 5 min. The AWACs also measured wave parameters of significant wave height (H_s, m), dominant period (T_p, s) and wave direction (θ_{dom}) every 60 min in 5 min bursts. Four Aquatec 210-TY loggers with Seapoint 880-μm optical backscatter sensors (OBS) were deployed at the three shallow stations and at the deep station at the headland apex; these instruments sampled backscatter every 5 min in 30 s bursts.

3.1.2. Bed sediment collection

To characterize the seabed adjacent to instrument locations and close to the apex of the headland, 17 grab samples were collected during the deployment along four shore-normal transects using a Van Veen sampler (Fig. 2). Approximately 500 g of sample was collected from each station and bagged for grain size analysis.

3.1.3. Additional data sources

The Santa Monica Bay NDBC buoy #46221 (Coastal Data Information Program, CDIP station #028) is approximately 23 km southeast of Pt. Dume at a depth of 363 m. Hourly observations of wave height, period, and direction were acquired from 18 September to 6 December 2014. Wind data were downloaded from the Santa Monica Basin NDBC buoy #46025 (35 km southwest of Pt. Dume at a depth of 935 m) and the closest Weather Underground station on Point Dume, KCAMALIB17. Wind speed and direction were acquired over the same time frame although the data were in different resolutions (NDBC buoy – hourly, Weather Underground station – 5 min). Bed sediment grain sizes were extracted from the usSEABED database (Reid et al., 2006) at nine locations in the study area.

3.2. Data processing

The time series of wave, current, and suspended sediment data, and the seafloor sediment samples were processed to determine alongshore flux under different forcing conditions. Through the processing described below, slightly less than 74 days of data were acquired as 1771 discrete points every 5 min. Background oceanographic conditions were characterized from the waves and currents and specific events (i.e., local storms) were identified. The processed data were packaged into inshore and offshore bands based on the spatial array of the instruments.

3.2.1. Wind and waves

The shoreline wind record at Pt. Dume was subsampled hourly to align with the offshore buoy wind record and other measured parameters (tides, waves, currents, and turbidity). The wave data from the two AWACs (T1 and T5) were initially processed by manufacturer software to convert raw acoustic returns to wave height, direction and period. The output time series were despiked using a phase-space method with a cubic polynomial to interpolate across removed outlier points (Goring and Nikora, 2002). The cleaned significant wave height (H_s, m) and dominant period (T_p, s) were used to calculate wave power (P, kW/m) for the shallow-water stations (T1 and T5) according to

$$P = \frac{1}{8}\rho g H_s^2 \sqrt{gh} \tag{1.1}$$

where ρ (kg/m^3) is water density, h is water depth (m), and g is gravity (m/s^2). Wave power at the deep-water buoy (B2) was calculated using the deep-water wave equation that replaces $\sqrt{gh}$ with $C_o = gT_p/2\pi$. The potential velocities for wave-driven longshore currents (V_L, m/s) were calculated using the Larson et al. (2010) method for wave height (H_b) and angle (θ_b) at breaking and applying them to the USACE (1984) equation

$$V_L = 20.7m\sqrt{gH_b}\sin(2\theta_b) \tag{1.2}$$

where m is the bed slope. In addition, wave-driven alongshore sediment transport, Q_c (m^3/yr), was also calculated using the CERC equation (USACE, 1984)

$$Q_c = 2.2 \times 10^6 \frac{H_b^{5/2}}{\gamma_b^{1/2}} sin(2\theta_b) \tag{1.3}$$

where $\gamma_b = H_b/h_b$.

3.2.2. Currents

Similar to the wave data, current data from the ADCPs (T2-T4 and T6) and AWACs (T1 and T5) were processed initially with manufacturer software to convert raw acoustic returns to speed and direction. The data were then rotated to true north and subsampled to obtain hourly data using a cubic spline function. The near-surface bins were removed by applying an echo intensity threshold of 60%, determined through an iterative process (M. Robart, BML, pers. comm.), below which data quality degraded due to bubbles and side-lobe reflection off the air-

water interface. The bottom bin that corresponded to 1 m above the bed (mab) was used to index near-bottom flow. The bin size was either 0.25 m (T2, T3, T4, T6) or 0.5 m (T1, T5). Following the guidance of Emery and Thomson (2001), the data were filtered at frequencies of 6 h (0.1667 cph) and 33 h (0.0303 cph) to separate subtidal (low-passed), tidal/diurnal (band-passed) and high-frequency variability. Local alongshore and cross-shore directions were determined based on the bathymetric contours and shoreline orientation: positive alongshore velocity was oriented 130° at T1 and T2, 90° at T3 and T4 and 60° at T5 and T6 (and positive cross-shore velocities at 40°, 0°, and −30°, respectively).

3.2.3. Bed shear stress

The total shear stress (τ_{total}, N/m^2) on the bed is a non-linear combination of wave-derived shear stress (τ_w, N/m^2) and current-derived shear stress (τ_{cur}, N/m^2). Total shear stress could only be calculated at stations T1 and T5 where wave data were collected in addition to currents. A routine following Madsen (1994) was used to calculate all three shear stresses that utilized time series of current velocity (U, m/s) and direction (θ_c, rad), a reference height for U (z_0, m), H_s, T_p, wave direction (θ_w, rad), h, temperature (T, °C), salinity (S, psu), seabed mean sediment grain size (D_{50}, m), and seabed sediment grain density (ρ_{sed}, kg/m^3). The process determines bed roughness (assuming a Nikuradse roughness of two times D_{50}), the angle between θ_c and θ_w, near-bottom orbital velocity, and angular wave frequency to calculate the friction velocity for currents, waves, and combined waves-currents. Shear stresses were then calculated by multiplying the square of friction velocity by the density of the seawater for a final output of τ.

3.2.4. Bed sediment

Sediment samples were washed twice with distilled water and then dried for 48 h at 30 °C. Grain size analyses were conducted using photogrammetric methods developed by Buscombe et al. (2010), where multiple images of the dried sediment are processed with Matlab algorithms. This technique has been employed successfully (through high significant correlations with sieving methods) for coastal environments in California and the United Kingdom (Buscombe et al., 2014), Portugal (Baptista et al., 2012) and New Zealand (Pentney and Dickson, 2012). Five photographs were taken for each sample with the sediment stirred between pictures because grain size can vary within a single sample. Sediment grain size statistics generated by the algorithm (mean, standard deviation, as well as the 5th, 16th, 25th, 75th, 84th, 90th, and 95th percentiles) for the five photographs were averaged to produce a distribution at each station.

3.2.5. Turbidity and flux

The OBS data (T1, T3, T4, and T5) were downloaded and despiked following the same methods as for the wave records to remove obvious erroneous data points. Gaps from the despiking were filled using a cubic spline and the cleaned time series were subsampled to hourly averages

to align with the wave and current data. The data at T3 were unusable due to biofouling on the optical window within a week of deployment. To develop turbidity estimates at T2 (where no OBS instrument was deployed) and T3 (no data returns), ADCP data at T4 was used following the method detailed by Deines (1999) as both ADCPs had the same frequency as T4. This is a two-step process that first calculates relative backscatter, S_v, to correct the acoustic backscatter data for signal spreading with distance from the transducers and for absorption by the water and then develops a regression relationship to the optical backscatter data to apply to other locations. Successful examples of this method include Holdaway et al. (1999), Thorne et al. (1991), and Storlazzi and Jaffe (2008). The regression at T4 had $R^2 = 0.30$, which is considered acceptable for this method (although low). Acoustic suspended sediment concentration (SSC) was estimated at T2 and T3 using the T4 regression relationship; acoustic SSC was calculated at T1 and T5 using the OBS and backscatter measurements at those stations. No turbidity or acoustic SSC time series are available at T6 because no OBS was deployed at this station and the ADCP used a different frequency than the other moorings. Total cumulative suspended sediment flux consisting of both along and cross-shore components ($\overrightarrow{SSF_{total}}$) was calculated by combining instantaneous flow velocities and acoustic SSC values in the following process:

$$\overrightarrow{SSF_{total}} = \sum_{t=1}^{1,771} \left(Acoustic\ SSC \times \overrightarrow{Flow_{along}} + Acoustic\ SSC \times \overrightarrow{Flow_{cross}} \right)$$

(1.4)

3.3. Additional analysis

Several analyses were designed to best utilize the data for addressing the research questions. To analyze for differences in sediment transport under different oceanographic conditions, events were isolated in the hydrodynamic (waves and tide) records and the subsequent sediment flux tallied at the inshore and offshore stations. Dividing the sediment volume by the duration normalized the relative impact of each event in sediment transport per day. To determine if there were differences on either side and across the apex of the headland, the flow directions and sediment flux at the inshore and offshore stations within the three geographic regions (exposed, apex, protected) were characterized by frequency of alongshore currents and by flux of sediment. Regional patterns of flow and transport were then used to assess qualitatively which flow scenario or scenarios describe the sediment pathways according to the criteria presented in Section 1.

4. Results

4.1. Identifying events

Regional average wave conditions over the collection period were $H_s = 1.03$ m ± 0.31, $T_p = 12.0$ s ± 2.8, and $\theta_w = 244° ± 30$ with

Table 3
Events during deployment.

Event	Start (2014, local time)	End (2014, local time)	Duration (d)	H_s[a] (m)	T_p[a] (s)	θ_{dom}[a] (°)	Tidal Range[b] (m)	Wind Speed[c] (m/s)	Wind Direction[c] (°)
Full Record	9/21, 0:00	12/3, 18:00	73.75	1.03 ± 0.31/2.23	12.0 ± 2.8/20.0	244 ± 30/338	2.21	3.26 ± 1.99/12.3	226 ± 92/-
Spring Tides	11/5, 17:00	11/8, 17:00	3.00	0.66 ± 0.09/0.91	13.0 ± 2.3/20.0	234 ± 30/289	2.21	3.07 ± 1.46/6.2	267 ± 103/-
Neap Tides	11/11, 9:00	11/14, 9:00	3.00	0.77 ± 0.08/1.02	13.0 ± 1.5/16.7	252 ± 11/282	1.38	2.81 ± 1.51/7.2	260 ± 45/-
Hurricane Simon	10/7, 10:00	10/9, 2:00	1.67	1.14 ± 0.17/1.53	12.0 ± 2.1/16.7	172 ± 20/209	2.05	2.00 ± 1.16/4.0	200 ± 100/-
Winter Storm	11/20, 0:00	11/22, 0:00	3.00	1.54 ± 0.23/2.23	11.1 ± 2.1/14.3	266 ± 6/282	2.16	4.53 ± 2.03/8.9	249 ± 99/-
Aleutian Low	10/25, 12:00	10/29, 0:00	3.50	1.28 ± 0.26/1.86	11.8 ± 2.1/15.4	253 ± 30/285	1.88	3.10 ± 2.18/8.6	250 ± 62/-

[a] Mean ± 1 Std. Dev /Maximum at Station B1.
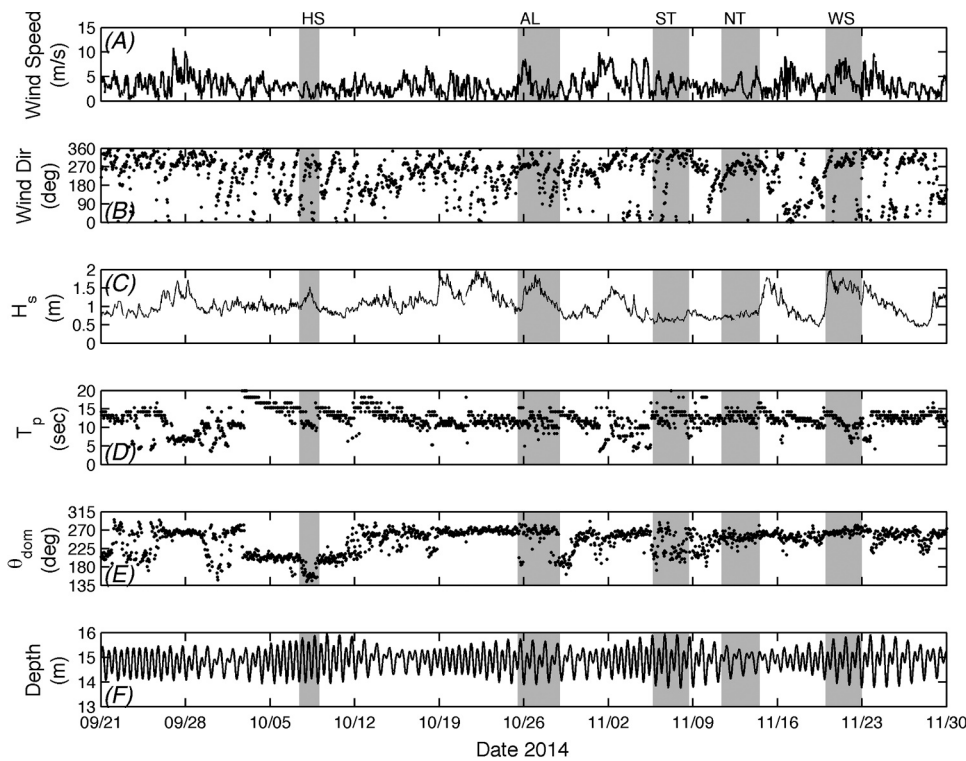[b] Range at Station T2.
[c] Mean/Maximum at Station B2.

Fig. 3. Regional conditions during the deployment of the instruments for wind speed and direction at B2 (*A, B*), wave height, period, and direction at B1 (*C, D, E*), and tide at T2 (*F*). Specific events are noted (Hurricane Simon – HS, Aleutian low – AL, spring tide – ST, neap tide – NT, and winter storm – WS). The hurricane is identified by the change in wave direction to mostly south and the increase in wave height. The Aleutian low event and winter storm are mostly evident in the wave height and wind speed. The tidal events were selected when wave height was the smallest of the record.

Table 4
Wave observations and longshore current calculation.

Station	Parameter	Range	Mean ± 1 std. dev
B1	H_s (m)	0.44–2.23	1.03 ± 0.31
	T_p (s)	3.12–20.00	12.00 ± 2.8
	θ_{dom} (°)	72°–338°	244° ± 30
	P (kW/m)	0.18–6.96	1.33 ± 8.3
T1	H_s (m)	0.41–1.65	0.84 ± 0.22
	T_p (s)	4.02–17.83	12.74 ± 2.40
	θ_{dom} (°)	175°–257°	222° ± 14
	P (kW/m)	0.19–3.03	0.85 ± 0.45
	V_L (m/s)	− 1.92 to 1.88	− 0.06 ± 1.07
T5	H_s (m)	0.27–1.87	0.62 ± 0.18
	T_p (s)	5.00–18.40	13.32 ± 1.69
	θ_{dom} (°)	146°–220°	198° ± 9.0
	P (kW/m)	0.09–4.35	0.53 ± 0.37
	V_L (m/s)	− 0.74 to 0.72	0.00 ± 0.38

wind speed of 3.26 m/s ± 1.99 and direction of 226° ± 92; the largest tidal range through the semi-diurnal mixed tide cycle was 2.21 m (Table 3). However, notable events occurred, with larger waves, winds or currents. These specific time periods were identified to investigate sediment transport under five different physical forcing scenarios (Fig. 3): (i) spring tides with low waves, (ii) neap tides with low waves, (iii) a large south swell event in early October from Hurricane Simon, (iv) a large NW swell event associated with a distant North Pacific Aleutian low pressure system in late October, and (v) a winter storm in late November (Table 3). Hurricane Simon was a category 4 hurricane that occurred 1–7 October 2014 off the west coast of Mexico, making landfall as a tropical storm in Baja California Sur (Stewart, 2014). South swell began arriving on 2 October and lasted for approximately eight days, although the largest waves lasted for less than two days (Fig. 3). During the Aleutian low event, NOAA charts from the Pacific Wind Wave Analysis and Pacific Surface Analysis Preliminary (http://nomads.ncdc.noaa.gov/ncep/charts) showed a large low pressure system with sea level atmospheric pressure of 985 mb and H_s of more than 8 m off the California coast on 24 October. The waves struck Santa Monica Bay from the west on 25 October and lasted about three days.

The same NOAA charts showed a series of winter storms arriving in southern California in late November that resulted in enhanced wave activity – the first three days were selected for analysis (Fig. 3).

4.2. Wind

The wind magnitude and direction at the two wind stations reflect their offshore (B2) and coastal (PD Wind) positions. Wind at the offshore station B2 was stronger with velocities exceeding 4 m/s and few calm periods (Table 3). The shoreline station PD Wind, exhibited a weaker mean but marked daily sea breezes, with onshore afternoon winds of 2–4 m/s. The strongest winds occurred at both stations during the winter storm, exceeding 5 m/s at B2 and 2.5 m/s at PD Wind. The principal axis due to diurnal winds is east-west at B2 and southwest-northeast at PD Wind.

4.3. Wave climate

The wave climate was characterized by H_s, T_p, θ_w data from the Santa Monica Bay buoy (B1) and the two AWACs located on the exposed (T1) and protected (T5) sides of the headland (Table 4). Wave activity was largest at the buoy where H_s exceeded 2 m and T_p reached 20 s while the lowest overall wave activity was recorded at the protected side of the headland. The wave direction was fairly consistent by station with westerly waves at the buoy, southwesterly waves on the exposed side, and south-southwesterly waves on the protected side of the headland. During Hurricane Simon, waves at the buoy came from the south and south-southeast, a marked deviation from typical conditions. Wave period lengthened to 15–20 s during the first part of the hurricane (2–5 October), followed by peaks in wave height associated with the southerly shift in wave direction (7 and 8 October). The larger of the peaks occurred approximately three-quarters through the event when waves came from the south-southeast. During the Aleutian low event, wave height increased suddenly with accompanying increases in wave period for all stations. A similar pattern was observed during the winter storm with some of the largest wave heights of the record (~2 m) measured at all three stations (Fig. 3 and Fig. 8).
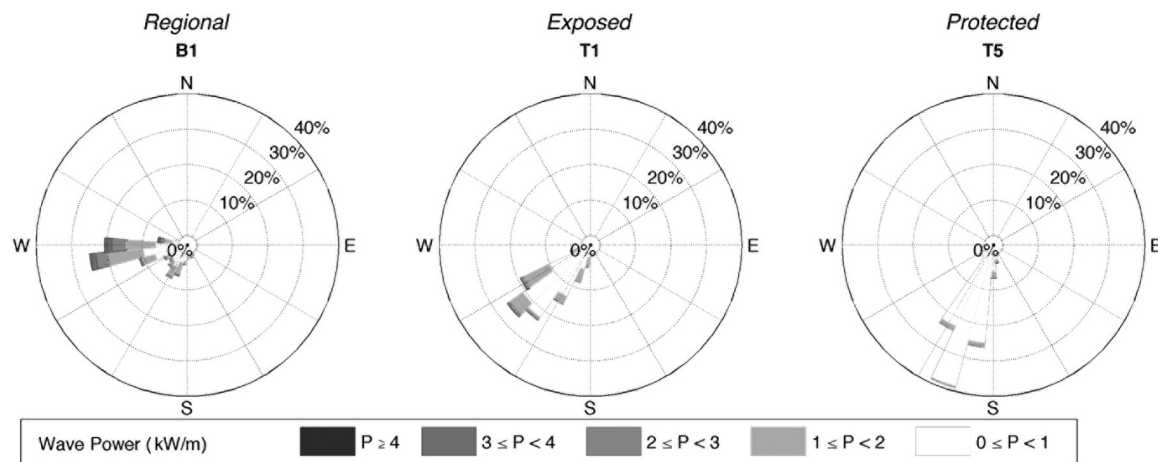
Fig. 4. Hourly wave power for the 74 days of the study. Data for B1 (regional) were downloaded from NOAA online sources; data at T1 (exposed) and T5 (protected) were from deployed AWACs. Wave power is largest at B1 and comes primarily from the west. Closer to land, wave power at T1 is larger with more of a southwest origin than T5.

The majority of wave power, P, at the buoy originated from the west and exceeded 2 kW/m approximately 10% of the time (Fig. 4). A small event of low P (< 2 kW/m) came from mostly the southwest during Hurricane Simon with approximately one day of energy originating from the south-southeast towards the end of hurricane swell. Wave power at the buoy peaked during the winter storm at more than 6 kW/m. On the exposed side of the headland, P was polarized in the southwest sector mostly between 210° and 240° and did not exceed 3 kW/m. The largest peak occurred during the Aleutian low with observable increases during the hurricane and winter storm (Fig. 8a). The protected side of the headland showed the smallest amount of P, never exceeding 2 kW/m and polarized entirely in the south-southwest sector mostly between 180° and 210°. The wave events produced less pronounced deviations in P from typical conditions on the protected side with one exception. During the hurricane, P spiked briefly for less than a day coincident with a shift in swell direction to south-southeast at the buoy (8 October; Fig. 8b). The estimated longshore current speed (V_L) reinforces the large difference between the two sides of the headland with ranges from −1.92 to 1.88 m/s on the exposed side and from −0.74 to 0.72 m/s on the protected side.

4.4. Near-bottom currents

Near-bottom currents at the six stations over the duration of the deployment show markedly different patterns between sites: exposed,

apex, or protected and inshore or offshore (Table 5). Current roses show that flow at exposed moorings (T1 and T2) was predominantly to the southeast, whereas on the protected side there is a difference between inshore (T5) with flow to the southwest and offshore (T6) with flow to the south (Fig. 5). Both sides showed dominant flow toward the apex with the inshore stations more clearly demonstrating this pattern than the offshore stations. When currents were decomposed into alongshore and cross-shore directions, the strong apex-ward currents on the west side were more evident (Fig. 6). On the exposed side, 74–76% of the time currents flow toward the apex whereas on the protected sides, apex-ward flow occurred 64–79% of the time (Table 6). Flow across the apex was more symmetrical in direction, although the inshore station showed more inward flow (53%) than the offshore station (43%). However, the flow patterns at the apex were bi-modal with eastward and southwestward modes inshore (T3) and westward and southeastward modes offshore (T4). The fastest speeds occurred near the apex, exceeding 0.2 m/s approximately 20% of the time.

4.5. Sediment: bed distribution

The overall bed sediment distribution was coarse sand to the west of the point and in shallow water depths with fining to the east and towards deeper water (Fig. 7). Sediment grain size nearshore was sand-dominated, even at the station located in the head of Dume Canyon (Table 7). Around the apex, D_{50} ranged from 0.196–0.572 mm with

Table 5
Near-bottom current velocities and turbidity.

Station	Currents			Acoustic SSC (kg/m³)	
	Parameter	Mean ± 1 std. dev	Maximum[a]	Range	Mean ± 1 Std. Dev
T1	Speed (m/s)	0.08 ± 0.05	0.32	3.76–5.81	4.60 ± 0.26
	Direction (°)[b]	174° ± 83	–		
T2	Speed (m/s)	0.07 ± 0.04	0.29	0–1.39	0.66 ± 0.24
	Direction (°)	184° ± 83	–		
T3	Speed (m/s)	0.13 ± 0.09	0.65	0–2.55	1.13 ± 0.41
	Direction (°)	153° ± 81	–		
T4	Speed (m/s)	0.13 ± 0.09	0.66	0–2.48	0.96 ± 0.39
	Direction (°)	205° ± 83	–		
T5	Speed (m/s)	0.08 ± 0.04	0.26	1.99–3.95	3.11 ± 0.26
	Direction (°)	194° ± 67	–		
T6	Speed (m/s)	0.13 ± 0.08	0.57	–	–
	Direction (°)	176° ± 96	–		

[a] Current direction showed all 360°.
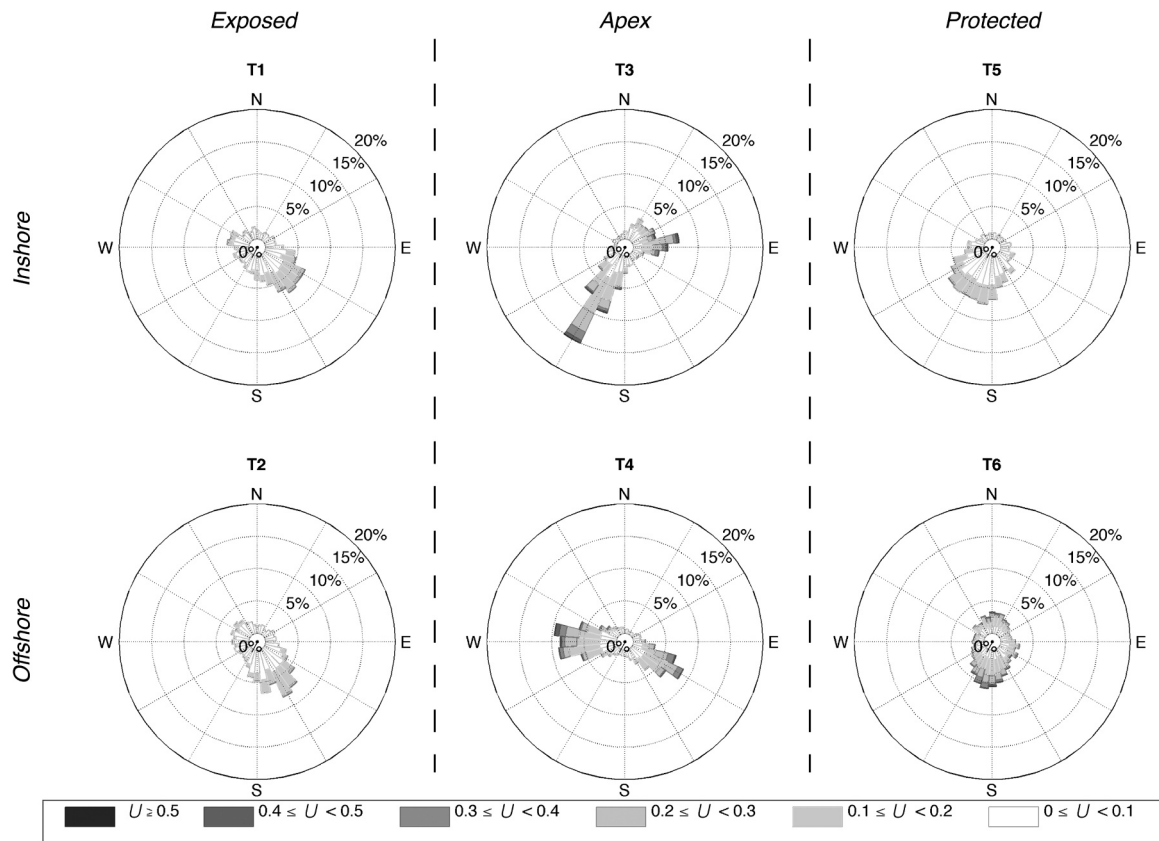[b] Current flowing towards.

Fig. 5. Hourly unfiltered near-bottom current velocities from the deployed current meters (ADCPs at T2, T3, T4, and T6; AWACs at T1 and T5). Dominant flow on the exposed side (T1 and T2) is to the southeast and on the protected side (T5) to the southwest and south (T6). Flow is fastest and switches direction across the apex (T3 and T4).

spatial patterns in the cross-shore and east-west directions. Three of the four shallow (5 and 8 m) stations on the exposed side of the headland were coarse sand with $D_{50} > 0.500$ mm (L1A, L1B, and L2B). This contrasted with the medium sand at the equivalent depths on the protected side and at the apex (L3A, L3B, L4A, and L4B). Sediment farther offshore and in the canyon became considerably finer to muddy sand or sandy mud. Below 15 m, grain size was finer across all transects as a shift to medium sand occurred on the exposed side. On transects L1 and L4 (the two farthest from the apex) at 25 m, the bed sediment decreased in size to fine sand with $D_{50} < 0.250$ mm. The finest sample of the 17
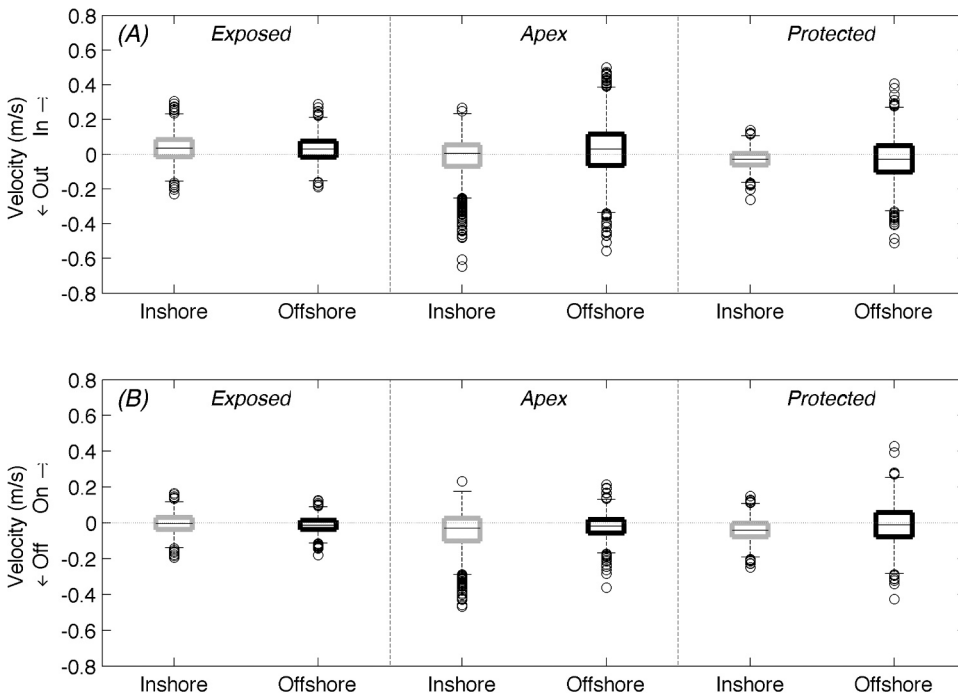

Fig. 6. Alongshore (*A*) and cross-shore (*B*) current velocities for the current meters divided into exposed, apex, and protected transects and by inshore (gray boxes) and offshore (black boxes) stations. On each box, the black line is the median, the edges of the box are the 25th and 75th percentiles, the whiskers extend to the most extreme data points not considered outliers, and outliers are plotted individually as circles.

Table 6
Alongshore and cross-shore current occurrence.

Station	Alongshore occurrence (%)[a]		Cross-shore occurrence (%)[b]	
	In	Out	Onshore	Offshore
T1	74	26	67	33
T2	76	24	62	38
T3	53	47	42	58
T4	43	57	48	52
T5	21	79	80	20
T6	36	64	67	33

[a] In and Out defined as crossing the apex into or out of Santa Monica Bay.
[b] Onshore and Offshore defined as shoreward or oceanward flow direction.

grabs was in the head of the canyon with $D_{50} = 0.196 \pm 0.01$ mm. The usSEABED samples farther from the headland that are deeper and to the east show $D_{50} < 0.125$ mm or finer (Reid et al., 2006).

4.6. Bottom shear stress and suspended sediment concentration

Wave-driven shear stress dominated 98% of the time over that due to currents at stations where both wave and current data were available. The strong connection between τ_{total} and the waves became apparent when tripling of τ_{total} was observed on the exposed side during the hurricane, Aleutian low and winter storm events, regardless of alongshore current velocities (Fig. 8a). This same station experienced markedly larger τ_{total} than on the protected side even though the current velocities were comparable. Underwater video of the seafloor taken during deployment and recovery of the instruments on the exposed side confirmed that the bed is in near-constant motion from surface waves even during the low-energy waves that allowed diving. Peak τ_{total} on the protected side occurred during the hurricane when wave direction was sufficiently southerly to impact the coastline directly (Fig. 8b). The other large wave events caused less pronounced increases in τ_{total} on the protected side. The general contrast between the headland sides is to be expected based on the 30° difference in dominant wave angle described in Section 4.3, which is due to refraction around the apex. In terms of

Table 7
Surface sediment grabs.

Station	Longitude (°W)	Latitude (°N)	Depth (m)	$D_{50} \pm 1$ Std. Dev(mm)
L1A	−118.81666	34.00783	5	0.512 ± 0.050
L1B (T1)	−118.81735	34.00736	8	0.572 ± 0.056
L1C (T2)	−118.81886	34.00628	15	0.383 ± 0.013
L1D	−118.82215	34.00383	25	0.244 ± 0.025
L2A	−118.81189	34.00275	5	0.443 ± 0.028
L2B	−118.81243	34.00249	8	0.507 ± 0.030
L2C	−118.81378	34.00171	18	0.378 ± 0.016
L2D	−118.81405	34.00122	26	0.294 ± 0.010
L2E	−118.81515	34.00049	45	0.196 ± 0.005
L3A	−118.80506	33.99945	7	0.449 ± 0.018
L3B (T3)	−118.80512	33.99890	11	0.379 ± 0.012
L3C (T4)	−118.80501	33.99719	16	0.326 ± 0.039
L3D	−118.80502	33.99416	25	0.299 ± 0.041
L4A	−118.79958	34.00423	5	0.319 ± 0.021
L4B (T5)	−118.79802	34.00320	10	0.290 ± 0.006
L4C (T6)	−118.79476	33.99914	17	0.288 ± 0.014
L4D	−118.79193	33.99705	26	0.232 ± 0.015

potential sediment suspension, τ_{total} remained above the threshold of motion as determined for the grain sizes collected from the bed at both inshore stations at all times. For the remaining 2% of bed shear stress due to currents solely, the tidal and subtidal components were each responsible for close to 50% of the forcing based on the filtered current data (Fig. 8a, b) while high frequency forcing accounted for less than 2%.

The hourly fluctuations throughout the acoustic SSC time series were expected from the dissipation of wave energy in the surf zone. The shear stresses and different D_{50} caused distinctive responses at the off-apex inshore sites. The lower bound of acoustic SSC on the exposed side was close to the upper bound on the protected side (Table 5). The time series on the exposed side showed clear increases in SSC associated with large wave events, but not so on the protected side (Fig. 8a, b). Spatially around the headland, acoustic SSC showed higher values at the inshore stations than offshore and lowest overall at the apex (Fig. 10), despite higher wave and current energy. The inshore exposed station showed the highest turbidity among all the stations with a mean of 4.60 kg/m³
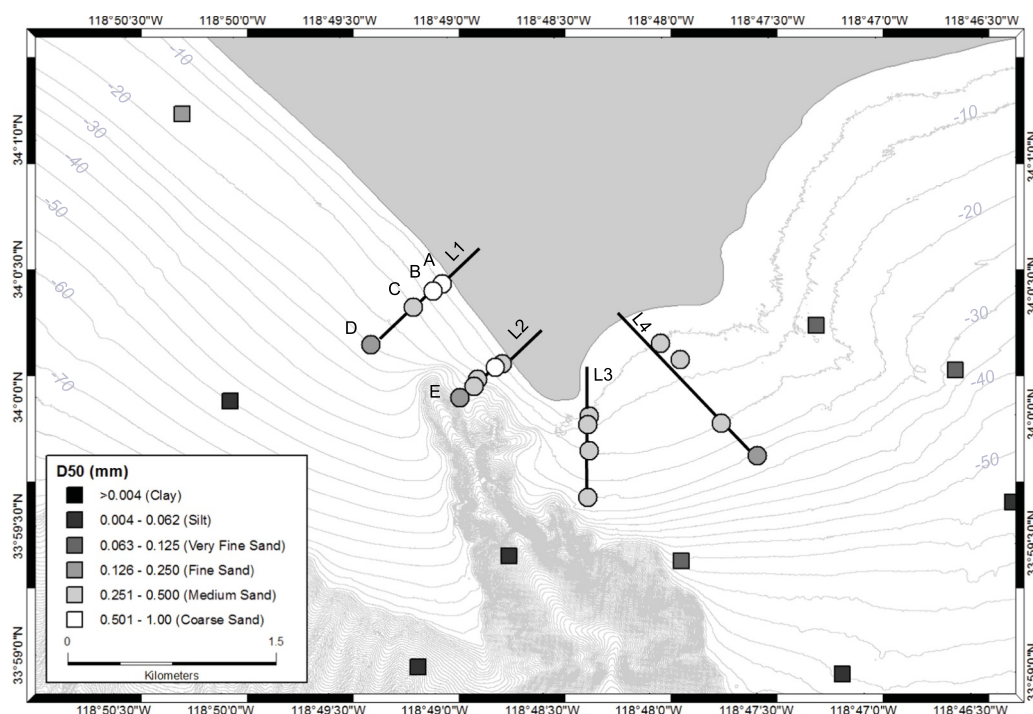

Fig. 7. Surface sediment grain size, D_{50}, from this study (circles along 'L' transects) and the usSEABED database (squares).
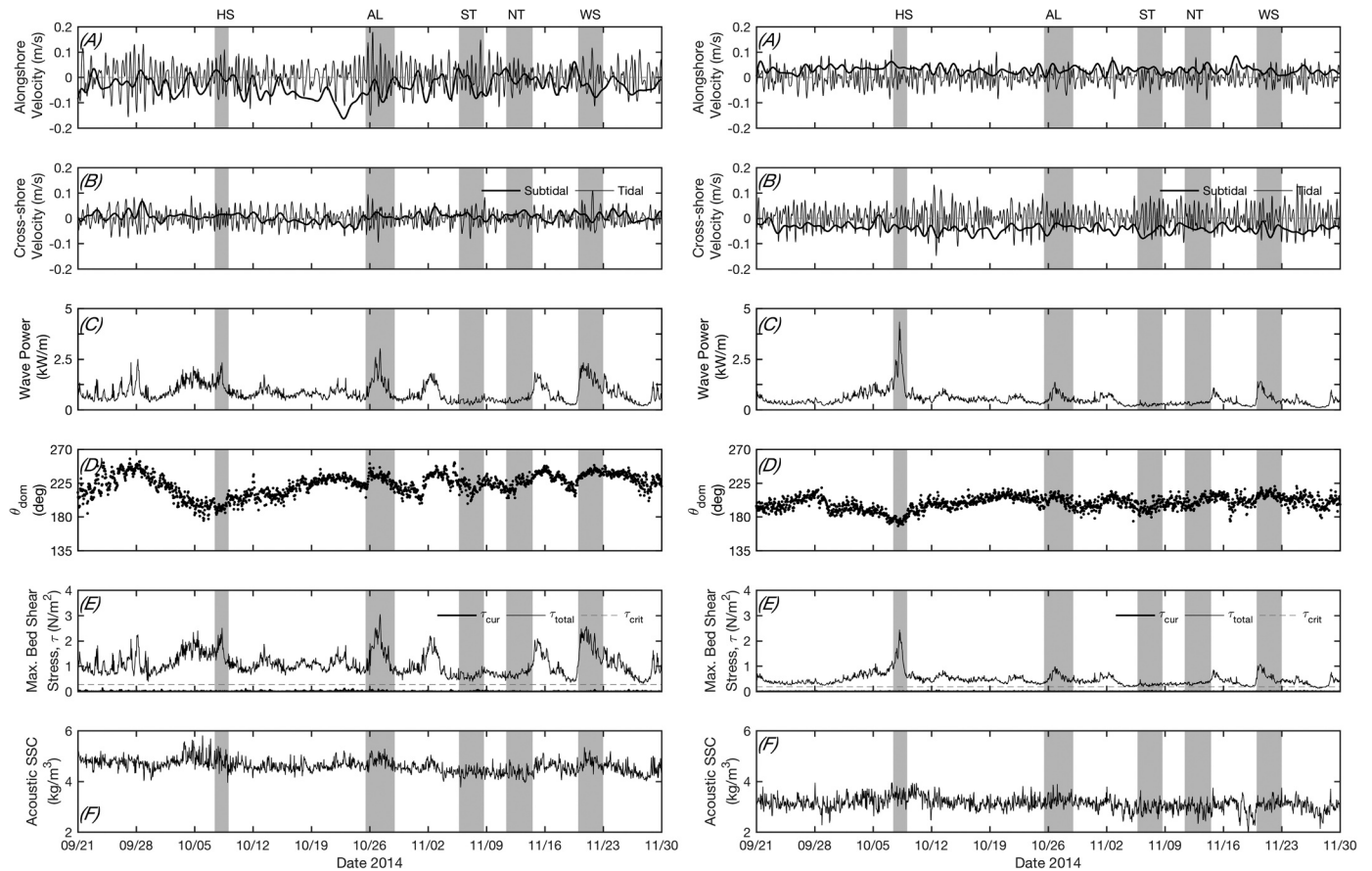
Fig. 8. Near-bottom alongshore (*A*) and cross-shore currents (*B*), wave power (*C*) and direction (*D*), maximum bed shear stress (τ_{total}, *E*), and acoustic SSC (*F*) at (a) the inshore exposed station (T1) and (b) inshore protected station (T5). See Fig. 3 for event identifications. For τ_{total}, current- (τ_{cur}) and wave-driven (τ_w) shear stress are combined with the threshold of motion (τ_{crit}) indicated as the dashed line for the specific grain size collected on the bed at each station.

Table 8
Cumulative sediment transport, SSF_{total}, (kg/m^2) at inshore stations, 1 mab.

Cumulative Total[a]	Regional Mean n/a	Exposed 293			Apex 113			Protected 282		
Events	Per day[a]	Event Total	Per day[a]	Direction	Event Total	Per day[a]	Direction	Event Total	Per day[a]	Direction
Hurricane	3.1 ± 1.4	2.85	1.7	205°	5.1	3.1	156°	7.49	4.5	231°
Aleutian low	4.3 ± 2.6	20.1	6.7	98°	4.8	1.6	208°	13.4	4.5	217°
Winter storm	4.0 ± 1.2	15.9	5.3	101°	9.0	3.0	273°	11.1	3.7	203°

[a] For duration, see Table 3.

with a large drop to a mean of 0.66 kg/m^3 at the offshore station. This gradient was steeper than that on the apex transect where the means and ranges were similar for both stations (Table 5). No gradient could be determined without an accompanying offshore station on the protected transect. Total cumulative suspended sediment flux (SSF_{total}) showed similar patterns with the highest values at the inshore stations compared to the offshore and the inshore exposed station the largest overall SSF_{total} (Fig. 10, Table 8). SSF_{total} at the inshore apex station was roughly one-third of the other two inshore stations. Both exposed stations and the offshore apex station showed flux to the east-southeast while the flux was to the southwest at other moorings.

4.7. Summary of results: sediment flux around Pt. Dume

While the results of waves, currents, suspended sediment, and seafloor sediment grain size provided an overall characterization of conditions at Pt. Dume, observations of SSF_{total} and daily rates of transport at the three inshore stations were most useful to directly address the

research questions (Table 8). SSF_{total} was not available for all three offshore stations. The daily sediment transport rates for different oceanographic conditions showed that the Aleutian low and winter storm events were more effective than the hurricane (4.0–4.3 vs. 3.1 kg/m^2/d). However, each event demonstrated spatial variability that reflected the origin of the event itself. The transport on the exposed side of the headland was largest for the Aleutian low and smallest for the hurricane (6.7 and 1.7 kg/m^2/d, respectively). This contrasted with the transport rates on the protected side of the headland where the hurricane and Aleutian low were the largest, and winter storm smaller (4.5 and 3.7 kg/m^2/d, respectively). Across the apex, which showed the lowest values of the three regions, the hurricane and winter storm were the largest and the Aleutian low, the smallest (3.0–3.1 and 1.6 kg/m^2/d, respectively). The transport decreased across the apex compared to either side of the headland for the winter storm and Aleutian low, but was larger than the exposed side during the hurricane. The direction of flux during the events was also spatially variable with the protected side ranging from 203° to 231°, the apex from 156° to 273°, and the

exposed side from 98° to 205°. Flux was consistently toward the apex on the protected side for all events and headed onshore on the exposed side from west-originating events (winter storm and Aleutian low). The apex showed flux from the protected side toward the exposed side for the winter storm, whereas it was reversed during the hurricane and off-shore for the Aleutian low.

5. Discussion

5.1. Near-bottom flow and sediment flux

The near-bottom circulation pattern around Pt. Dume can be characterized as apex-ward flow from both sides, with reversing flow at the apex (Table 6). The timing and differing velocities of the reversals develops flow convergence zones on either side of the headland. The alongshore flow on the exposed side appears to separate whereas on the protected side, a back eddy forms. This back eddy is likely enhanced by refraction of the waves around the headland that generates wave-driven flows. The observed 30° difference in dominant wave angle is consistent with refraction processes that would also alter the orbital velocities and flow directions. One example is within a California-wide analysis of wave energetics by Erikson et al. (2014) in which modeled results around headlands show enhanced orbital velocities as flow shifts direction from refraction under identical forcing conditions. At Pt. Dume for the current study, two modes of overall flow can be identified as Scenarios A and B in Fig. 1 based on the time series at the six stations when wave-driven flows are combined with the tidal and subtidal flows (Fig. 9). A pattern which occurred 42% of the time arises when alongshore flow is "in" (eastward) on the exposed side, "out" (westward) on the protected side, and "out" across the apex (Fig. 9) – which appears to represent Scenario A, with an outward flow separating and forming an offshore jet, but it is possible that a flow structure like Scenario B may also exhibit itself in this way, with the outward flow reattaching to the shore further west. Scenario A is also more likely for

outflow because of the wave forcing along the exposed side of the headland that enhances separation and may allow the separated flow to remain detached. Another pattern, which occurred 41% of the time, arises when alongshore flow is "in" on the exposed side, "out" on the protected side – but flow is "in" across the apex. This pattern represents separation of inward flow at the apex and while it may also by a manifestation of Scenario A, it appears to be more consistent with Scenario B in which an eddy forms (accounting for westward flow at T5 and southward flow at T6) before the flow reattaches to the shoreline further east. The absence of forcing on the sheltered side of the headland suggests that the westward flow is driven by the eddy (headland wake). Although there are not wave data at the apex, it is probable that the flow separation zone is a more balanced mix of wave-driven and tidally-derived currents compared to the off-apex areas where wave-driven flow dominates. For the remaining 17% of the time the flow patterns are mixed between A and B. Continuous flow from one side to the other never occurs (neither in nor out), thus eliminating Scenario C which represents attached flow.

Together, the flow and wave conditions at Point Dume are expected to yield circulation and sediment transport that is thus a blend of Scenarios A and B. Time-varying patterns may appear complex, but these appear to be the dominant modes of flow. However, the presence of a submarine canyon plays an obfuscating role and its effects were not part of this study. The sediment pathways speculated here suggest possible transport of fine suspended particles into the eddy east of the headland during inward flow, but termination of coarse sediment transport at the apex of the headland with some medium sediment exported offshore. Conversely, outward flow is unlikely to be transporting coarse sediment in the absence of wave forcing on the sheltered side of the headland. Finer sediment that may remain in suspension is likely to be exported offshore, settling out at depth in and beyond the canyon. The bed sediment D_{50} seems to support this expectation by being coarse along the route of a probable offshore jet on the exposed side and finer under the eddy on the protected side. The spatial pattern
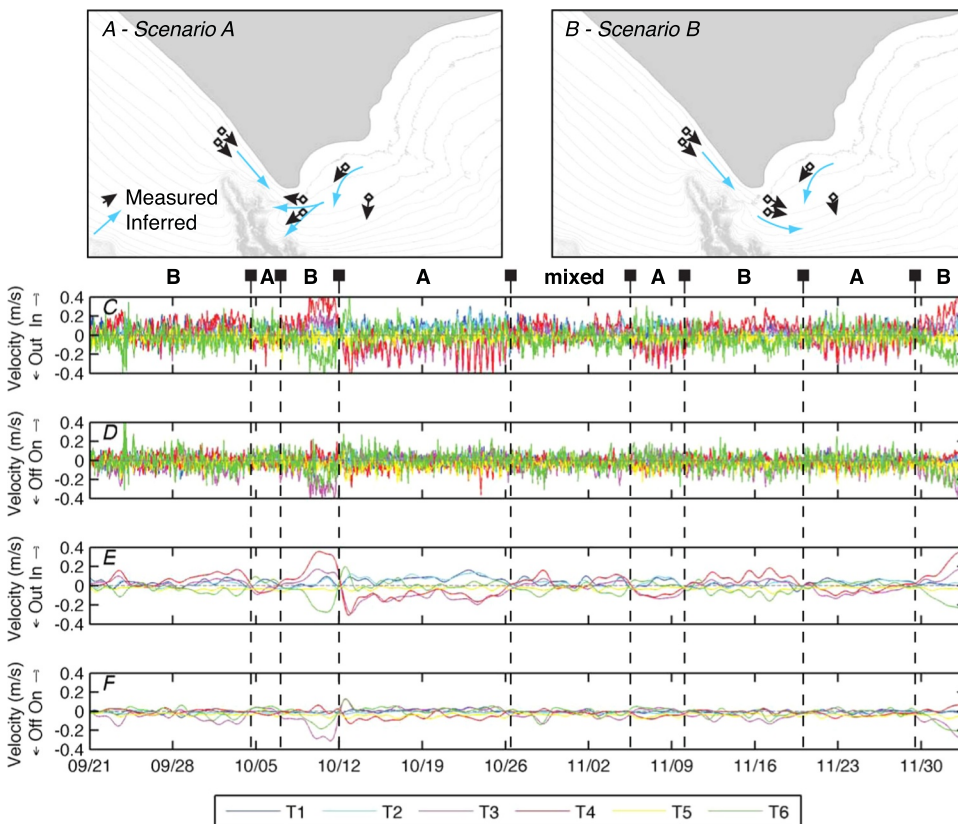

Fig. 9. Near-bed circulation in space (*A*, *B*) and through time (*C-F*) to identify flow scenarios presented in Fig. 1. In *A* and *B*, the black arrows represent measured direction of flow and blue are inferred currents for each scenario. Unfiltered time series of alongshore (*C*) and cross-shore (*D*) flow show tidal pulsing during the two scenarios. Subtidally filtered time series of alongshore (*E*) and cross-shore (*F*) flow allow sharper identification of the scenarios. The longevity of scenario type (A or B) is indicated by the zones between the dashed vertical lines.
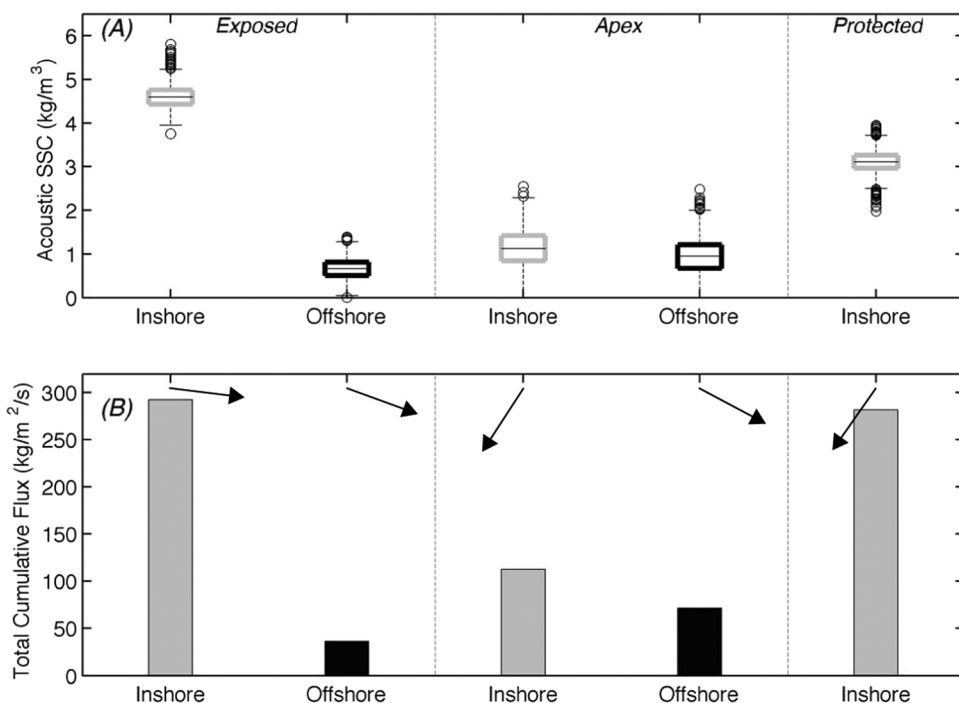
Fig. 10. (*A*) Acoustic SSC divided into exposed, apex, and protected transects and by inshore (gray boxes) and offshore (black boxes) stations. On each box, the black line is the median, the edges of the box are the 25th and 75th percentiles, the whiskers extend to the most extreme data points not considered outliers, and outliers are plotted individually as circles. (*B*) Cumulative total suspended sediment flux (columns) by inshore (gray) and offshore (black) stations with direction of mean flux (arrows).
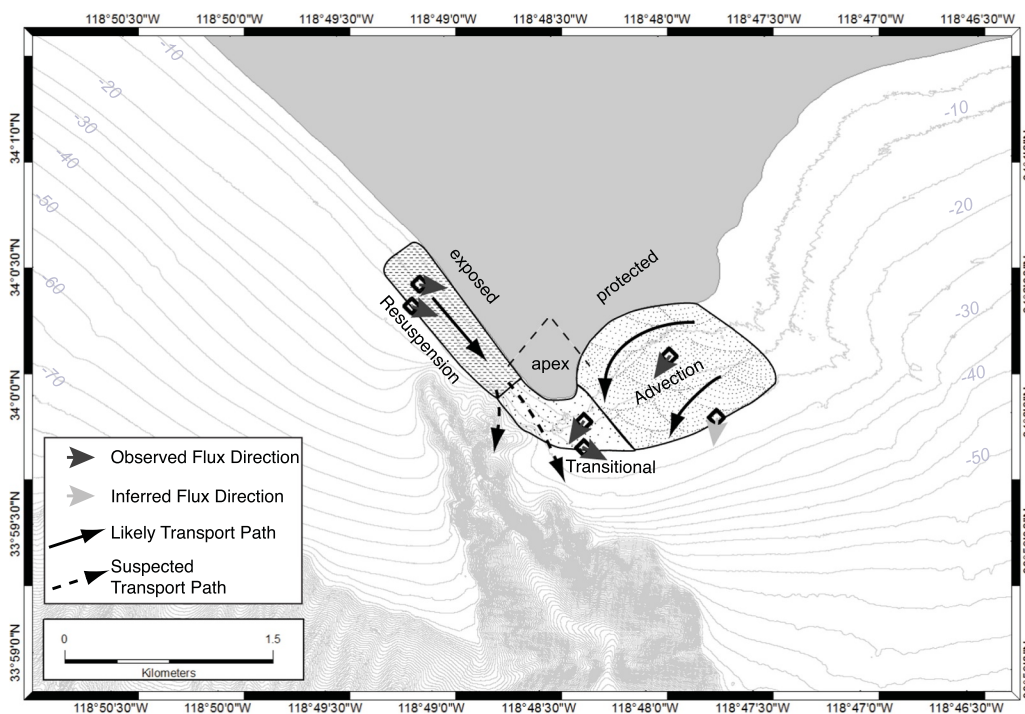
Fig. 11. Conceptual model of sediment transport pathways around the tip of Pt. Dume with resuspension, transitional, and advection regions. Transport is complicated by the head of the canyon off the exposed side of the headland. Sediment traveling alongshore on the exposed side would likely be ejected at the apex following Scenario A whereas on the protected side, an eddy and dominant wave direction allows deposition following Scenarios B (Fig. 1).

in SSF_{total} at the inshore stations reaffirms the speculated pathways by showing that flux at the apex station is only a third of that at either the exposed or protected station (Fig. 10). An important caveat to this interpretation is that the pathways are likely ephemeral in their location and behavior by meandering or broadening through time. This type of pattern in the sediment transport is similar to that observed at Cape Rodney in New Zealand where sediment transport pathways differed on different sides of the headland (Hume et al., 2000). The canyon may be altering the sediment supply by allowing removal of coarse sediment (Everts and Eldon, 2005) in transit toward the apex from the exposed side, although the flux direction at the apex offshore station aligns with the probable jet direction (Fig. 11).

Despite the canyon, the separation of flux in magnitude and direction suggests three regions for sediment transport around a headland that falls into Scenarios A and B. The zone on the exposed side is the most energetic from waves, which leads to high turbidity and flux (Table 8). The central zone at the apex is transitional where tidal currents have intensified but decreased sediment availability causes flux that is almost one-third that of the other regions. The protected zone experiences a decrease in both wave and tidal energy but the finer bed sediment is more readily advected, resulting in an increase in flux compared to the transitional zone.

Underpinning these zones is the variation in longshore currents and wave-driven transport across the surf zone. Transport in all of the
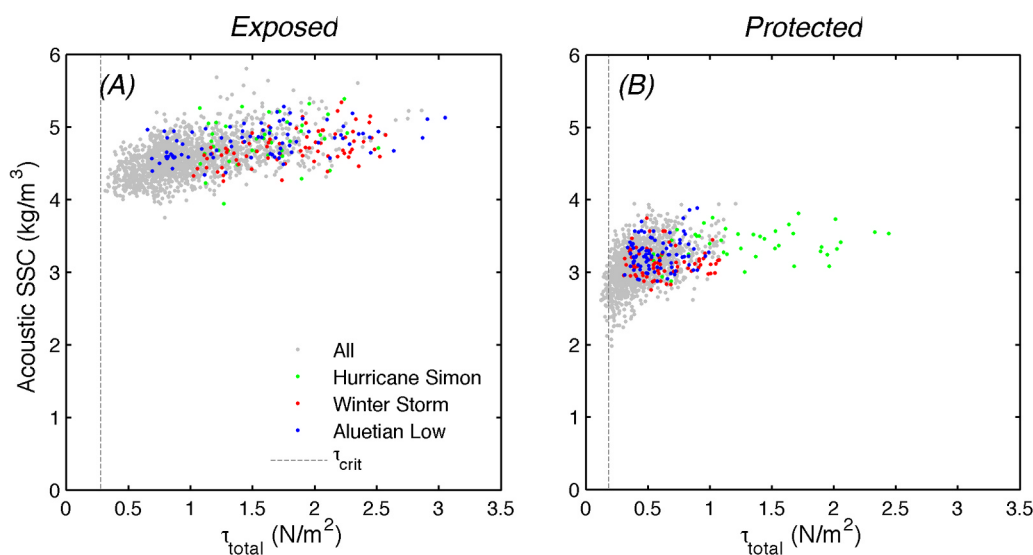
Fig. 12. Relationship between τ_{total} and acoustic SSC on the exposed (*A*) and protected (*B*) sides of the headland with large wave events highlighted and the threshold of motion (τ_{crit}) indicated as the dashed line for the specific grain size collected on the bed at each station. On the exposed side, acoustic SSC increases when τ_{total} increases whereas on the protected side, there is not a clear relationship.

regions is connected to the grain size with fining in the offshore direction as bed shear stress decreases. The magnitude of the currents and subsequent transport is largest on the exposed side before bed friction and coastal geometry have deformed the waves. Refraction around the headland reduces the energy available for generating the requisite shear stresses to resuspend bed sediment. The spatial variation in τ_{total} and response in turbidity is easily seen between the exposed and protected sides (Fig. 12). The τ_{total} and acoustic SSC relationship is more correlated on the exposed side with $R^2 = 0.26$ ($p < 0.01$ for $n = 1771$) compared to the protected side with $R^2 = 0.17$ ($p < 0.01$ for $n = 1771$), although neither are particularly strong. Even so, resuspension is likely the dominant process on the exposed side with larger waves and longshore current whereas suspended sediment concentrations are better explained by advection (import) on the protected side. The spatial differences are clearer when large wave events are isolated. For example, during the Aleutian low event, the exposed side shows a better correlation ($R^2 = 0.20$, $p < 0.01$ for $n = 85$) and higher total flux (20.1 kg/m²/s) than on the protected side where the correlation is insignificant ($R^2 = 0.02$, $p = 0.17$ for $n = 85$) and total flux is lower (13.4 kg/m²/s). When the wave direction shifted during the hurricane, total flux was more than twice as large on the more protected side compared to the exposed side (Table 8).

5.2. Headland as a barrier to littoral drift

Pt. Dume was initially described as the terminal point for the Santa Monica Littoral Cell (Habel and Armstrong, 1978), because of its size, proximity to Dume Canyon, and the regional geography. As mentioned earlier, subsequent studies by Inman (1986), Orme (1991), and Knur and Kim (1999) attempted to quantify how the point-canyon complex affects alongshore transport of sand, with estimates of 10–90% of sediment bypassing the headland and being lost in the canyon. After Patsch and Griggs (2007) conducted a review of existing studies to create a sediment budget for the littoral cell, a new perspective emerged that described the headland as an internal boundary between two sub-cells. The current study partially supports that contention. If the circulation patterns follow Scenario A/B, jets would shunt certain grain sizes offshore at the headland apex but the canyon removes most of the larger grain (e.g., sand) fractions. This creates a sorting effect, where the fine grain sediment (e.g., mud) that remains in suspension may transit around Pt. Dume, while the coarser sediment is transported offshore. Summarizing the likely dynamics at Pt. Dume by grain size, we conclude that the headland is: (i) unlikely to see westward wave-driven transport of coarse sand past headland; (ii) eastward sand

transport is expected to separate at the apex where some may deposit in the canyon or otherwise in an offshore deposition zone; (iii) eastward flux of mud is likely to be entrained in the eddy and deposit in the eddy zone; and (iv) westward flux of fine particulates may be pushed back or moved in the jet offshore.

From a narrow definition of a littoral cell that only considers sand, Pt. Dume is a significant barrier. However, if the full distribution of sediment grain sizes in the area is considered, Pt. Dume is likely to be only a partial, coarse-grain preferential barrier. The concept of sorting sediment grain sizes within a littoral cell was explored by Limber et al. (2008) using a littoral cell cutoff grain size diameter, or the minimum sand grain size found on the beaches of a cell. The idea that a headland could shift between barrier types aligns with Scenario B (a large downstream zone that may not receive coarse sediment, but in which finer sediment may accrete due to weaker currents) in that shifting oceanographic conditions can disrupt the typical pathways. The flow separation and transitional zone at the apex indicate how and where the different grain sizes detach from each other.

Taking a further step on how the interaction of the headland shape and flow dynamics affect the littoral cell boundary, Pt. Dume may be a barrier to sediment transport on a seasonal basis. One example of this response can be found in Goodwin et al. (2013) who identified that when the dominant wave direction at Cape Byron, Australia, shifted 20°, sediment transport changed significantly around the headland in both the longshore and cross-shore directions. Seasonal shifting was explored by George et al. (2015), who found that periodic shifts in wave energy determine the efficacy of a littoral cell boundary. In their classification, Pt. Dume was found to be a partial boundary. A more canyon-specific study of the physical and geological processes at the head of the canyon under different conditions would help clarify the sediment pathways both spatially and temporally.

6. Conclusion

Sediment transport around a rocky headland was examined through a field experiment that focused on sediment pathways that are dependent on flow and wave direction. Waves, currents, turbidity, and bed sediment gathered at the field location, Pt. Dume, California, revealed that transport is a blend of three conceptual models. Through wave and near-bottom current observations, the flow was characterized as most often directed towards the point from either side of the headland with flow separation at the apex. On the more exposed side of the headland, wave-driven longshore currents are stronger and bed shear stress is larger resulting in resuspension and high suspended sediment flux

toward the apex. On the more protected side of the headland, finer bed sediment and lower velocities indicate a less dynamic region where advection likely plays a larger role in flux than resuspension. Sediment is unlikely to transit across the apex where despite the fastest velocities, sediment supply is limited by probable ejection of sand from the exposed side. The transport of any sediment around the headland depends on the grain size by separating into either deposition zones on the shelf or into Dume Submarine Canyon (sand) or alongshore and offshore transport (mud). From this study, Pt. Dume could be a mixed barrier to sediment depending on grain size and season, which suggests it is a partial littoral cell boundary. Other headlands with comparable morphologies or hydrodynamics could be investigated with similar techniques to better characterize natural barriers to littoral drift.

Acknowledgements

References

Baptista, P., Cunha, T.R., Gama, C., Bernardes, C., 2012. A new and practical method to obtain grain size measurements in sandy shores based on digital image acquisition and processing. Sediment. Geol. 282, 294–306.

Bastos, A.C., Kenyon, N.H., Collins, M., 2002. Sedimentary processes, bedforms and facies, associated with a coastal, headland: portland Bill, Southern UK. Mar. Geol. 187, 235–258.

Berthot, A., Pattiaratchi, C., 2006. Field measurements of the three-dimensional current structure in the vicinity of a headland-associated linear sandbank. Cont. Shelf Res. 26, 295–317.

Black, K., Oldman, J., Hume, T., 2005. Dynamics of a 3-dimensional, baroclinic, headland eddy. N.Z. J. Mar. Freshw. Res. 39, 91–120.

Buscombe, D., Rubin, D.M., Lacy, J.R., Storlazzi, C.D., Hatcher, G., Chezar, H., Wyland, R., Sherwood, C.R., 2014. Autonomous bed-sediment imaging-systems for revealing temporal variability of grain size. Limnol. Oceanogr.-Methods 12, 390–406.

Buscombe, D., Rubin, D.M., Warrick, J.A., 2010. A universal approximation of grain size from images of noncohesive sediment. J. Geophys. Res. 115.

Davies, P.A., Dakin, J.M., Falconer, R.A., 1995. Eddy formation behind a coastal headland. J. Coast. Res. 11, 154–167.

Deines, K.L., 1999. Backscatter estimation using broadband acoustic doppler current profilers. RD Instruments Application Note FSA-008. pp. 1–5.

Emery, W.J., Thomson, R.E., 2001. Data Analysis Methods in Physical Oceanography. Elsevier, New York.

Erikson, L.H., Storlazzi, C.D., Golden, N.E., 2014. Modeling Wave and Seabed Energetics on the California Continental Shelf. Pamphlet to accompany data set., In: Survey, U.S. G. (Ed.), Santa Cruz, California.

Everts, C.H., Eldon, C.D., 2005. Sand capture In Southern California submarine canyons. Shore Beach 73, 3–12.

Freeland, H., 1990. The flow of a coastal current past a blunt headland. Atmos.-Ocean 28, 288–302.

George, D.A., Largier, J.L., Pasternack, G.B., Barnard, P.L., Storlazzi, C.D., Erikson, L.H., 2018. Modeling sediment bypassing around idealized rocky headlands. J. Mar. Sci. Eng.

George, D.A., Largier, J.L., Storlazzi, C.D., Barnard, P.L., 2015. Classification of rocky headlands in California with relevance to littoral cell boundary delineation. Mar. Geol. 369, 137–152.

Goodwin, I.D., Freeman, R., Blackmore, K., 2013. An insight into headland sand by-passing and wave climate. variability from shoreface bathymetric change at Byron Bay, New South Wales, Australia. Mar. Geol. 341, 29–45.

Goring, D.G., Nikora, V.I., 2002. Despiking acoustic Doppler velocimeter data. J. Hydraul. Eng.-Asce 128, 117–126.

Guillou, N., Chapalain, G., 2011. Effects of waves on the initiation of headland-associated sandbanks. Cont. Shelf Res. 31, 1202–1213.

Habel, J.S., Armstrong, G.A., 1978. Assessment and Atlas of Shoreline Erosion Along the California Coast. State of California, Department of Navigation and Ocean Development, Sacramento, CA, pp. 277.

Hickey, B.M., 1992. Circulation over the Santa-Monica San-Pedro Basin and Shelf. Prog. Oceanogr. 30, 37–115.

Hickey, B.M., Dobbins, E.L., Allen, S.E., 2003. Local and remote forcing of currents and temperature in the central Southern California Bight. J. Geophys. Res.-Oceans 108.

Holdaway, G.P., Thorne, P.D., Flatt, D., Jones, S.E., Prandle, D., 1999. Comparison between ADCP and transmissometer measurements of suspended sediment concentration. Cont. Shelf Res. 19, 421–441.

Hume, T.M., Oldman, J.W., Black, K.P., 2000. Sediment facies and pathways of sand transport about a large deep water headland, Cape Rodney, New Zealand. N.Z. J. Mar. Freshw. Res. 34, 695–717.

Inman, D.L., 1986. Southern California Coastal Processes Data Summary.

Klinger, B., 1993. Gyre formation at a corner by rotating barotropic coastal flows along a slope. Dyn. Atmos. Oceans 19, 27–63.

Knur, R.T., Kim, Y.C., 1999. Historical Sediment Budget Analysis along the Malibu coastline, Sand Rights '99- Bringing Back the Beaches. ASCE, Ventura, CA, pp. 292.

Larson, M., Hoan, L., Hanson, H., 2010. Direct formula to compute wave height and angle at incipient breaking. J. Waterw., Port., Coast., Ocean Eng. 136, 119–122.

Leidersdorf, C.B., Hollar, R.C., Woodell, G., 1994. Human intervention with the Beaches of Santa Monica ray. Calif. Shore Beach 62, 29–38.

Limber, P.W., Patsch, K.B., Griggs, G.B., 2008. Coastal sediment budgets and the littoral cutoff diameter: a grain size threshold for quantifying active sediment inputs. J. Coast. Res. 24, 122–133.

MacCready, P., Pawlak, G., 2001. Stratified flow along a corrugated slope: separation drag and wave drag. J. Phys. Oceanogr. 31, 2824–2839.

Madsen, O.S., 1994. Spectral wave-current bottom boundary layer flows. Coast. Eng. 1994, 24th Int. Conf. Coast. Eng. Res. Counc. 384–398.

Magaldi, M.G., Ozgokmen, T.M., Griffa, A., Chassignet, E.P., Iskandarani, M., Peters, H., 2008. Turbulent flow regimes behind a coastal cape in a stratified and rotating environment. Ocean Model. 25, 65–82.

Nickols, K.J., Gaylord, B., Largier, J.L., 2012. The coastal boundary layer: predictable current structure decreases alongshore transport and alters scales of dispersal. Mar. Ecol. Prog. Ser. 464, 17–35.

Noble, M.A., Rosenberger, K.J., Hamilton, P., Xu, J.P., 2009. Coastal ocean transport patterns in the central Southern California Bight. Earth Sci. Urban Ocean.: South. Calif. Cont. Borderl. 454, 193–226.

Orme, A.R., 1991. The Malibu coast – a contribution to the city-wide wastewater management study, p. 50.

Patsch, K., Griggs, G., 2007. Development of Sand Budgets for California's Major Littoral Cells. Institute of Marine Sciences, University of California, Santa Cruz, pp. 115.

Pattiaratchi, C., James, A., Collins, M., 1987. Island wakes and headland eddies: a comparison between remotely sensed data and laboratory experiments. J. Geophys. Res.: Oceans 92, 783–794.

Pentney, R.M., Dickson, M.E., 2012. Digital grain size analysis of a mixed sand and gravel beach. J. Coast. Res. 28, 196–201.

Reid, J.A., Reid, J.M., Jenkins, C.J., Zimmermann, M., Williams, S.J., Field, M.E., 2006. usSEABED: Pacific Coast (California, Oregon, Washington) Offshore Surficial-sediment Data Release.

Roughan, M., Mace, A.J., Largier, J.L., Morgan, S.G., Fisher, J.L., Carter, M.L., 2005. Subsurface recirculation and larval retention in the lee of a small headland: a variation on the upwelling shadow theme. J. Geophys. Res.-Oceans 110.

Short, A.D., 1999. Handbook of Beach and Shoreface Morphodynamics. John Wiley, New York.

Signell, R.P., Geyer, W.R., 1991. Transient Eddy formation around headlands. J. Geophys. Res.-Oceans 96, 2561–2575.

Soulsby, R., 1997. Dynamics of Marine Sands: a Manual for Practical Applications. Thomas Telford, London.

Stewart, S.R., 2014. Tropical Cyclone Report. Hurricane Simon (EP192014), In: National Hurricane Center, N. (Ed.), p. 18.

Storlazzi, C.D., Jaffe, B.E., 2008. The relative contribution of processes driving variability in flow, shear, and turbidity over a fringing coral reef: west Maui, Hawaii. Estuar. Coast. Shelf Sci. 77, 549–564.

Stul, T., Gozzard, J., Eliot, I., Eliot, M., 2012. In: Transport, W.A.Do (Ed.), Coastal Sediment Cells between Cape Naturaliste and the Moore River, Western Australia. Damara WA Pty Ltd and Geological Survey of Western Australia, Fremantle, WA, Australia, pp. 44.

Thorne, P.D., Vincent, C.E., Hardcastle, P.J., Rehman, S., Pearson, N., 1991. Measuring suspended sediment concentrations using acoustic backscatter devices. Mar. Geol. 98, 7–16.

USACE, 1984. Shore Protection Manual. In: U. S. Army Corps of Engineers, C.E.R.C. Department of the Army, Waterways Experiment Station, Corps of Engineers, Vicksburg, pp. 656.

van Rijn, L.C., 2010. Coastal Erosion Control Based on the Concept of Sediment Cells. Conscience, Deltares, The Netherlands, pp. 80.

Verron, J., Davies, P., Dakin, J., 1991. Quasigeostrophic flow past a cape in a homogeneous fluid. Fluid Dyn. Res. 7, 1–21.

Wolanski, E., Pickard, G.L., Jupp, D.L.B., 1984. River plumes, coral reefs and mixing in the Gulf of Papua and the northern Great Barrier Reef. Estuar., Coast. Shelf Sci. 18, 291–314.

Xu, J.P., Noble, M.A., 2009. Variability of the Southern California wave climate and implications for sediment transport. Earth Sci. Urban Ocean.: South. Calif. Cont. Borderl. 454, 171–191.